C. R. Chimie 22 (2019) 525–533

Contents lists available at ScienceDirect

Comptes Rendus Chimie

www.sciencedirect.com

Full paper/Mémoire

Effects of solvent vapor annealing on the crystallinity and spin crossover properties of thin films of $[Fe(HB(tz)_3)_2]$

Effets d'un recuit en présence de vapeurs de solvant sur la cristallinité et les propriétés de transition de spin d'un film mince de $[Fe(HB(tz)_3)_2]$

Alin-Ciprian Bas [a, b], Victoria Shalabaeva [a], Xavier Thompson [a], Laure Vendier [a], Lionel Salmon [a], Christophe Thibault [b], Gábor Molnár [a], Lucie Routaboul [a, *], Azzedine Bousseksou [a, **]

[a] LCC-CNRS, Université de Toulouse, CNRS, 31077 Toulouse, France
[b] LAAS-CNRS, Université de Toulouse, CNRS, INSA, 31077 Toulouse, France

ARTICLE INFO

Article history:
Received 18 October 2018
Accepted 13 March 2019
Available online 19 April 2019

Keywords:
Spin crossover complex
Solvent vapor annealing
Thin films
Crystallinity
UV-vis spectroscopy
X-ray diffraction

ABSTRACT

We investigated the solvent vapor annealing process of thermally evaporated thin films of the $[Fe^{II}(HB(tz)_3)_2]$ (tz = 1,2,4-triazol-1-yl) spin crossover complex. Using grazing incidence X-ray diffraction, atomic force microscopy, and variable-temperature UV spectrophotometry, we show how the crystallinity, morphology, and spin crossover properties of the resulting films are altered by exposure to vapors of five different solvents: diethyl ether, acetone, dichloromethane, ethanol, and water. Remarkably, most solvents yielded highly oriented crystalline films displaying an abrupt and complete spin transition around 336 K. A notable exception is the case of dichloromethane—suggesting that the solvent ability to accept hydrogen bonding might be a key factor in controlling the film crystallinity. On the other hand, only water vapor treatment affords for smooth and continuous film morphology. The recrystallization process in controlled humidity was thus followed in situ by monitoring the UV absorbance of the films. This study revealed the critical importance of the relative humidity (RH): for values above a threshold of ca. 72% RH (at 298 K) a very fast (seconds) crystallization occurs leading to robust, crystalline films, whereas crystallization at lower RH values is slower (hours) and leads to less stable, semicrystalline films displaying incomplete spin transitions.

Mots Clés:
Complexe à transition de spin
effets de vapeurs de solvant
films minces
cristallinité

RÉSUMÉ

Nous avons étudié le recuit en présence de vapeurs de solvant d'un film mince obtenu par évaporation thermique du complexe à transition de spin $[Fe^{II}(HB(tz)_3)_2]$ (tz = 1,2,4-triazol-1-yl). L'utilisation de la diffraction des rayons X à angle rasant, de la microscopie à force atomique et de la spectrométrie UV à température variable nous a permis de montrer l'évolution de la cristallinité, de la morphologie et des propriétés de transition de spin de

* Corresponding author.
** Corresponding author.
E-mail addresses: lucie.routaboul@lcc-toulouse.fr (L. Routaboul), azzedine.bousseksou@lcc-toulouse.fr (A. Bousseksou).

https://doi.org/10.1016/j.crci.2019.03.002

spectroscopie UV–vis
diffraction des rayons X

ces films minces après leurs expositions à différentes vapeurs de solvant (éther diéthylique, eau, acétone, dichlorométhane et éthanol). De façon remarquable, la majorité de ces solvants conduisent à des films cristallins (préférentiellement orientés) qui possèdent une transition de spin abrupte et complète à une température proche de 336 K. Cette étude montre que le dichlorométhane est une exception notable, ce qui suggère que la capacité du solvant à accepter les liaisons hydrogène pourrait être un facteur clé dans le contrôle de la cristallinité du film. Par ailleurs, seul le traitement en présence de vapeur d'eau conduit à un film peu rugueux et de morphologie régulière. Le procédé de recristallisation sous humidité contrôlée a aussi été suivi, in situ, par la mesure de l'absorbance dans l'UV de ces films. Cette étude révèle que l'humidité relative (RH) est un critère primordial : pour des valeurs autour de ou supérieures à 72% de RH (à $T = 298$ K), une recristallisation très rapide (à l'échelle de la seconde) s'effectue et conduit à un film cristallin, alors que la recristallisation réalisée avec des valeurs de RH plus basses mène à des films semi-cristallins qui sont moins stables et qui possèdent une transition de spin incomplète.

1. Introduction

Spin crossover (SCO) complexes exhibiting a reversible switching between their low-spin (LS) and high-spin (HS) electronic configurations have received considerable attention because of their fascinating ability to change magnetic, optical, electrical, and mechanical properties as a response to different external stimuli such as changes in temperature, pressure, intense magnetic field, and others [1–4]. Thanks to the recent progress in nanoscale organization of SCO compounds into films and nanoparticles, SCO materials have become very attractive for their implementation in nanosized devices for electronic, spintronic, photonic, and nanomechanical applications [2,5–9].

In this context, we have recently been extensively investigating the molecular SCO compound $[Fe^{II}(HB(tz)_3)_2]$ (tz = 1,2,4-triazol-1-yl) (**1**) [10]. It is characterized by an isostructural and abrupt first-order spin transition between its LS and HS configurations, above room temperature (ca. 333 K), with a narrow thermal hysteresis loop (ca. 2 K width) [11]. An optical microscopy study of the nucleation-growth dynamics of the spin transition in single crystals of **1** demonstrated exceptionally fast switching kinetics and a remarkable mechanical resilience upon repeated thermally induced spin transition [12]. Moreover, compound **1** was used to synthesize high-quality thin films by thermal evaporation under high vacuum conditions, providing films with a very high purity and tight thickness control [13]. This allowed us to investigate, in detail, the thickness dependence of the spin transition in the films [14]. The ability to feature continuous thin films, whose thickness can be tuned with nanometric precision, in combination with the spin transition just above room temperature, makes compound **1** very attractive for the implementation in nanoscale devices. Notably, crystalline thin films of **1** were integrated into micro-electromechanical systems in which the SCO molecules were used to tune the mechanical properties of the device and to perform controlled and reversible macroscopic work [15,16]. We also succeeded in fabricating large-area crossbar electrical junctions from thin films of **1,** in which we observed resistance switching upon the SCO [17]. Then, using liquid electrodes, resistance switching was demonstrated by Poggini et al. [18] in tunneling junctions of **1**.

It is important to stress that pristine thermally evaporated thin films of $[Fe(HB(tz)_3)_2]$ usually show poor environmental stability and stable reproducible films could be obtained only by postdeposition annealing. Indeed, the crystalline structure, morphology, and SCO properties of freshly deposited films significantly alter over time in ambient air, making them difficult to integrate as building blocks in nanodevices. To overcome this problem, we previously demonstrated that thin films of **1** with extremely robust SCO properties could be obtained by means of a simple solvent vapor annealing (SVA) process. Notably, the exposure of the freshly evaporated amorphous films to water vapor (ca. 75–80% relative humidity, RH) at room temperature led to very efficient and fast crystallization [13]. These crystalline films turned out to be remarkably stable in ambient air for long periods and over more than four SCO cycles.

In the present study, we systematically examined the crystallinity, morphology, and SCO characteristics of thin films of **1** after their exposure to the vapors of five different solvents: diethyl ether, acetone, dichloromethane, and water. $[Fe(HB(tz)_3)_2]$ films were characterized by means of grazing incidence X-ray diffraction (GIXRD), atomic force microscopy (AFM), and variable-temperature ultraviolet–visible (UV–vis) absorption techniques. The crystallization process upon water exposure was further investigated by *in-situ* absorbance measurements using a dedicated environmental chamber with simultaneous humidity and temperature control.

2. Experimental section

Reagents and solvents used in this study are commercially available. The bulk powder of **1** was synthesized as described in Rat et al. [11]. Thin films with thicknesses in the 100–200 nm range were grown by thermal evaporation in a custom-built film deposition system (PREVAC) at a base pressure of ca. 2×10^{-7} mbar. The bulk powder was heated until 250 °C in a quartz crucible and evaporated at a rate of 0.03 Å s^{-1}. The evaporation rate and film thickness were monitored in situ using a quartz crystal microbalance.

The final film thickness was determined using AFM. The films were deposited onto fused silica substrates, which were cleaned with acetone and isopropanol to remove contaminants. For SVA, we used five different solvents: diethyl ether, acetone, dichloromethane, ethanol, and water. After film deposition, the substrates with $[Fe(HB(tz)_3)_2]$ thin films were immediately placed in a sealed vial of 60 mL along with an open vial containing 10 mL of a given solvent. This led to a saturated solvent atmosphere in the large vial whereas direct contact between the film and the liquid was avoided. Except otherwise stated, annealing was carried out at room temperature for 10 min. Identical vials were used for each experiment thus leading to different saturated vapor pressures for the different solvents.

The GIXRD experiments were carried out in a PANalytical X'Pert PRO MPD system using Cu Kα radiation (45 kV and 40 mA) with a parallel-beam configuration. The incident beam optics consisted of a mirror with a 1/32° divergence slit. A parallel plate collimator (0.18°) and Soller slits (0.04°) were mounted on the path of the diffracted beam. An X'Celerator detector in receiving slit mode was used for X-ray collection. AFM surface topography measurements were done using a Cypher-ES microscope (Oxford Instruments) in amplitude-modulation mode, in ambient air using OMCLAC160TS-R3 (Olympus) probes. Optical microscopy images were acquired in reflectivity mode using a Motic stereomicroscope equipped with a digital camera. The temperature-dependent absorbance spectra of the thin films were collected at wavelengths between 250 and 800 nm using a Cary 50 (Agilent Technologies) spectrophotometer and a Linkam FTIR-600 heating–cooling stage, equipped with fused silica windows. The sample chamber was purged with dry nitrogen and spectra were acquired in the 293–393 K range with 1 K min^{-1} rate. For *in-situ* absorbance measurements, the heating–cooling stage was connected to a Linkam RH95 humidity controller, which allows for a fine control of the humidity around the sample between 5% and 90% RH.

3. Results and discussion

SVA, which consists of exposing a film to a solvent vapor at (or near) room temperature, has recently become an increasingly popular “mild” method to control thin film morphology and crystallinity. Considering that one can use various solvents with different solubility parameters and vapor pressure, SVA represents a highly versatile approach. In particular, the effects of solvent vapors on block copolymer films [19–22], organic semiconductor films [23–27], and compounds of pharmaceutical interest [28,29] have been described formerly. However, the effects of solvent vapors on SCO films were previously not much explored [13,30]. The effects of SVA mainly depend on the properties of applied solvents [23,24,26]. Solvent molecules interact with the surface of a material and, depending on solvent-material affinity, film permeability, morphology, exposure time, and temperature, the solvent can diffuse into it or condense on the surface and dissolve molecules. In either case, the “softening” of the material then enables movement and/or rearrangement of molecules.

The solubility of **1** is rather low in common solvents. Among those used in this study, diethyl ether, acetone, and ethanol can be considered as nonsolvents, whereas water and dichloromethane are “poor solvents” (ca. 1 mg/ml at 298 K). We have chosen these solvents with different polarities, vapor pressures, and hydrogen-bonding abilities to enable meaningful comparisons. Table 1 gathers some commonly used quantitative parameters describing these properties. In particular, the Hansen solubility parameters characterize the cohesive energy density of the substance, decomposed for dispersive interactions (δ_d), polar interactions (δ_p), and hydrogen-bonding contributions (δ_H). The vapor pressure (P_v), boiling point (T_b), and surface tension (γ) are also related to the cohesive forces between the solvent molecules, whereas the Gutmann donor number (DN) is used to quantify the Lewis basicity of solvents.

First, we analyzed by GIXRD the crystalline structure of the five solvent-exposed $[Fe(HB(tz)_3)_2]$ films of ca. 200 nm thickness. In the diffraction geometry used, only crystal planes parallel to the substrate can be observed. This allows probing the crystallinity (and crystal structure) and determination of the preferred crystal orientation. Fig. 1 shows the diffraction patterns of the solvent annealed films and the freshly evaporated film. One may notice that the initial featureless diffraction pattern of the amorphous pristine film drastically changes after exposure to the different solvents. Remarkably, the diffraction pattern of each solvent annealed film is dominated by a single, intense, and narrow peak at a 2θ value of 10.01°. We have previously reported this diffraction peak for the humidity annealed films and, by comparison with the XRD pattern of the bulk powder, we could unambiguously assign it to the 002 reflection [13]. This result denotes crystalline order and preferential orientation of the water-annealed film with the orthorhombic *c*-axis normal to the substrate (Scheme 1). Most likely, the films adopt this orientation because of the low surface energy of the 00*l* planes. The key experimental finding of the present work is that water is not the only solvent, which recrystallizes the films. However, one

Table 1
Solvent properties [31]: Hansen solubility parameters (dispersive, polar, and H-bonding) in units of MPa, vapor pressure (at 20 °C) in units of kPa, boiling point (at 1 atm) in units of °C, surface tension (at 20 °C in air) in units of mN/m, and Gutmann DNs in units of kcal/mol.

Solvent	δ_d	δ_p	δ_H	P_v	T_b	γ	DN
Water	15.5	16.0	42.3	3.17	100	72.8	18
Ethanol	15.8	8.8	19.4	5.95	78.3	22.1	32
Diethyl ether	14.5	2.9	4.6	58.7	34.6	17.1	19.2
Dichloromethane	17.0	7.3	7.1	57.3	39.8	26.5	1
Acetone	15.5	10.4	7.0	30.6	56.3	25.2	17

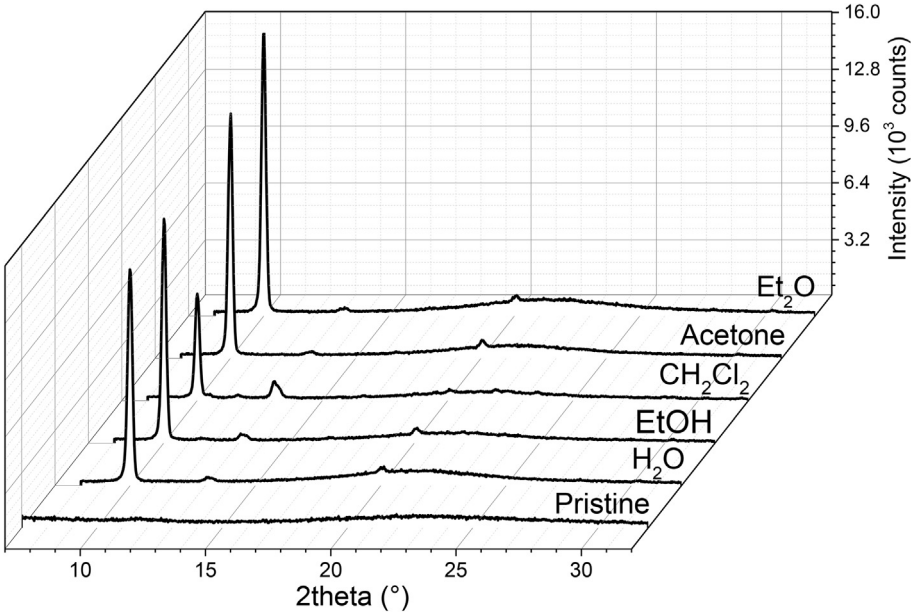

Fig. 1. XRD patterns of $[Fe(HB(tz)_3)_2]$ thin films exposed to different solvents. The diffractogram of a pristine film is also shown. (N.B. The broad peak around $2\theta = 15°–27°$ is typical for amorphous fused silica substrates used in this study [32]).

may notice that the film treated with CH_2Cl_2 exhibits a significantly weaker diffraction intensity at 10.01° in comparison with the films exposed to other solvents. In addition, the XRD pattern of the dichloromethane-exposed film exhibits other diffraction peaks with relatively high intensities (with respect to the main peak). These results denote that the crystallinity and ordering of the dichloromethane-annealed films is lower when compared with other samples.

To investigate how the different crystallinity of the films alter the SCO properties, we performed variable temperature optical absorption measurements over two heating–cooling cycles between 293 and 393 K. Fig. 2a shows selected UV absorbance spectra of the SCO thin films annealed with different solvents. The intense absorption bands between 260 and 340 nm are bleached upon increasing the temperature from 293 to 393 K, which can be explained by the SCO phenomenon. Fig. 2b

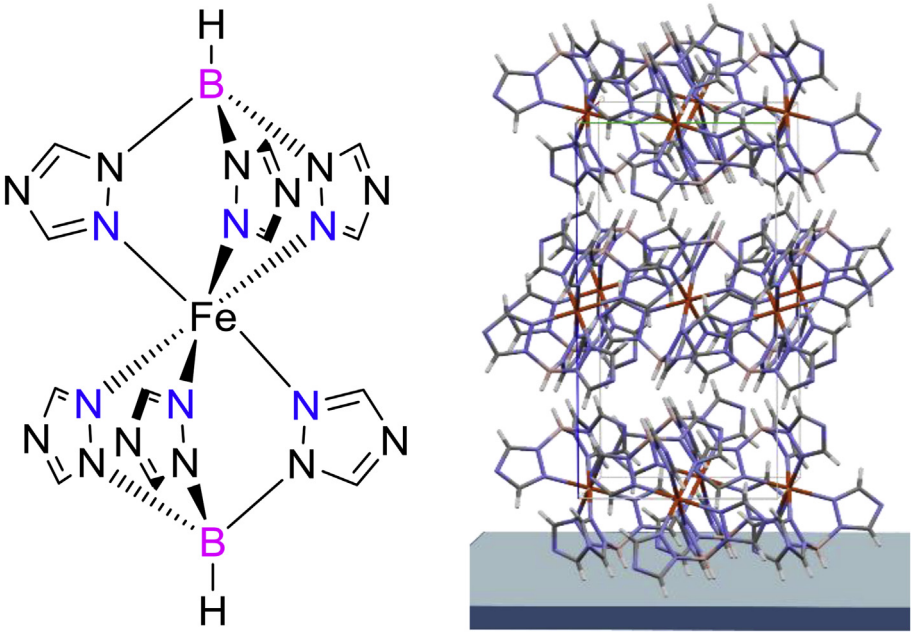

Scheme 1. (a) Molecular structure of $[Fe(HB(tz)_3)_2]$ and (b) its crystal structure in oriented thin films.

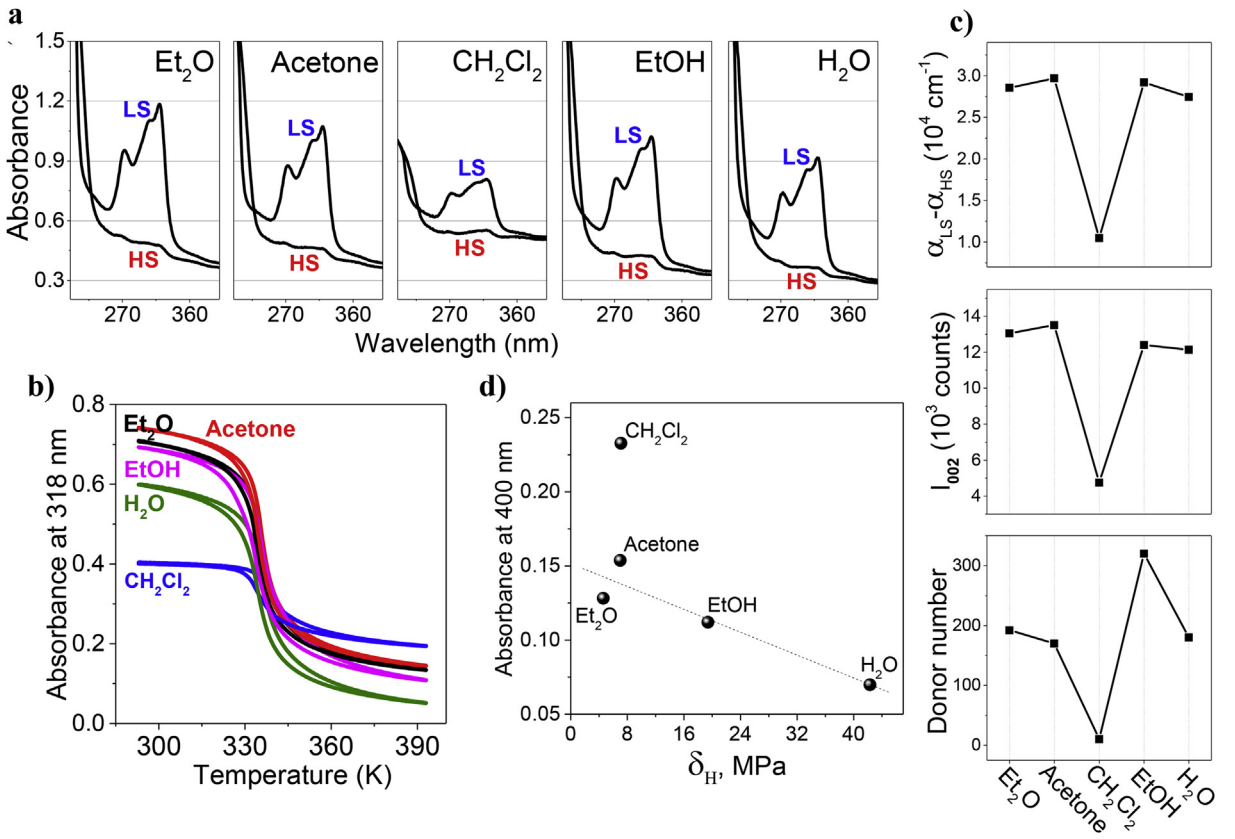

Fig. 2. (a) Absorbance spectra acquired at 293 K (LS) and 393 K (HS) in the heating mode for [Fe(HB(tz)$_3$)$_2$] films annealed with different solvents (uncorrected spectra). (b) Temperature dependence of the absorbance at 318 nm (baseline corrected) along the second heating–cooling cycle recorded at 1 K min^{-1} scan rate for different solvent-treated samples. (c) Absorbance coefficient change at the spin transition ($\lambda = 318$ nm), intensity of the 002 XRD peak (thickness normalized), and solvent DN for different solvent-treated samples. (d) Absorbance at 400 nm (baseline corrected) as a function of the Hansen solubility parameter δ_H.

displays the absorbance (at 318 nm) as a function of temperature for the different solvent-treated films. One may note that all films exhibit a rather abrupt spin transition with similar transition temperatures ($T_{1/2} \approx$ 336 K) and small hysteresis widths ($\Delta T \approx 2$ K) (see also Table 2). However, the shape and intensity of the absorption spectra of the CH_2Cl_2-treated sample is different from the others and the absorbance change upon the spin transition is drastically reduced in this sample indicating an incomplete SCO (ca. 36%). In addition, the absorbance change between the LS and HS states ($Abs_{LS} - Abs_{HS}$) and intensity of the XRD peak at $2\theta = 10.01°$ (I_{002}) are correlated for the different samples (see Fig. 2c and Table 2). These findings suggest that the lower degree of crystallinity and ordering could be the primary cause for the very incomplete spin transition in the CH_2Cl_2 vapor annealed sample.

Table 2
Properties of solvent annealed films: spin transition temperature, hysteresis width, absorption coefficient change upon the spin transition (at 318 nm), intensity of the 002 XRD peak (thickness normalized), UV–vis absorbance at 400 nm (baseline corrected).

Solvent	$T_{1/2}$ (K)	ΔT (K)	$\alpha_{LS} - \alpha_{HS}$ (10^4 cm^{-1})	I_{002} (counts)	Abs_{400nm} (baseline corrected)
Diethyl ether	335.6	1.6	2.85	13,000	0.13
Acetone	336.0	1.3	2.97	13,500	0.15
Dichloromethane	338.9	3.5	1.05	4740	0.23
Ethanol	335.7	3.1	2.92	12,400	0.11
Water	336.0	2.2	2.74	12,100	0.07

When comparing the properties of the different solvents used (see Table 1 and Fig. 2c), it appears that the poor crystallinity of the sample treated with dichloromethane and consequently its inferior SCO properties might be related to its low DN, that is, its low ability to accept hydrogen bonds, in comparison with the four other solvents used in our study. We can thus suggest that the SVA treatment of films of **1** is more efficient when the SCO molecules can form hydrogen bonds with the solvent molecules. Because **1** is much less soluble in diethyl ether/acetone/ethanol than in dichloromethane, the most plausible mechanism of SVA in the present case would be solvent diffusion into the film causing intermolecular hydrogen bonds to break. Then, the higher mobility of the SCO molecules can allow the pristine metastable film to evolve into a thermodynamically more favorable crystalline state.

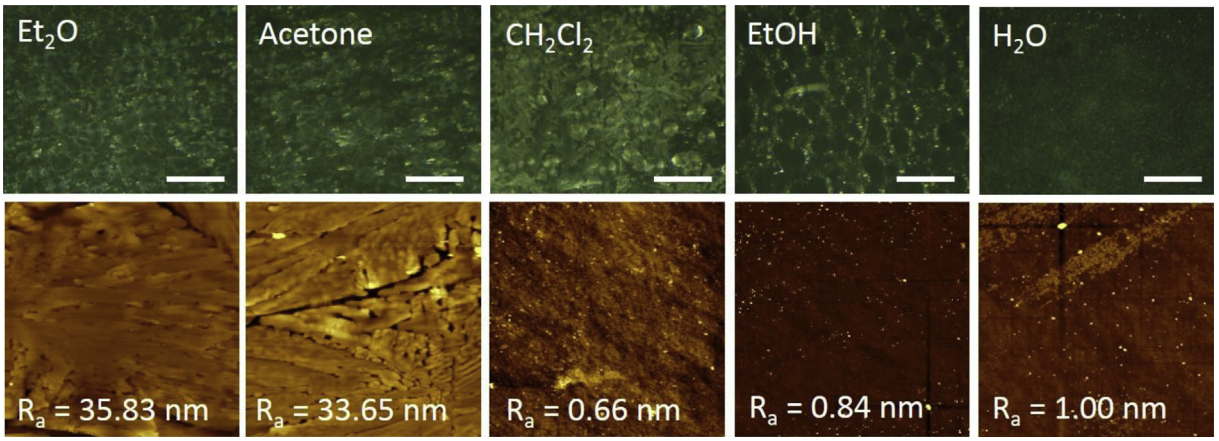

Fig. 3. Optical microscopy (top panel) and AFM surface topography (bottom panel) characterization of the different solvent vapor annealed [Fe(HB(tz)$_3$)$_2$] films. Scale bar in optical images: 500 μm; AFM image size: 30 × 30 μm [2].

Another interesting observation one can make about the absorption spectra in Fig. 2a and b of the different solvent-treated samples is their substantially different spectral baseline (see also Table 2). This finding denotes that the light scattering intensity of the films strongly differs, indicating that the morphology of the films must be different. To further investigate this aspect, we examined the surface morphology of different solvent-exposed [Fe(HB(tz)$_3$)$_2$] films using optical microscopy and AFM. Fig. 3 shows the optical and AFM topography images of the thin films after exposure to the solvents. The water-exposed [Fe(HB(tz)$_3$)$_2$] film is characterized by a smooth and continuous morphology, whereas the other samples appear more irregular. At first glance, the AFM topography images suggest that CH_2Cl_2 and EtOH-treated films are smooth, characterized by low values of arithmetic average roughness R_a. However, in this case the small area AFM topography analysis is not representative as optical images show the presence of some large-scale aggregates/crystals in these samples as well.

Interestingly, the light scattering intensity (i.e., the baseline of the absorbance spectra) is correlated with the Hansen solubility parameter δ_H of the solvents (Fig. 2d), denoting that the surface roughness decreases when δ_H increases. (N.B. The case of CH_2Cl_2 deviates from this trend, but we believe the deviation occurs because of its different crystallinity.) The solubility parameters of solvents have already been reported to be correlated with the changes in crystallinity and morphology of various organic films when exposed to the solvents [23,24,28,29,33]. In our case we can suggest that during SVA, water not only diffuses into the film as we suggested above for the different solvents, but for its lower vapor pressure, it may also condense on the surface of the pristine film. Because the solubility of **1** in water is not very high, fast supersaturation occurs and a large number of crystallization seeds form simultaneously, leading to densely packed, small crystallites and thus a smooth surface morphology. For the other solvents, larger crystals form, which indicates different film growth mechanism(s) involving possibly no surface condensation and less nucleation seeds.

Overall, we can conclude that the water vapor annealing gives the most efficient recrystallization procedure, offering the best control on film morphology, crystallinity, and SCO properties. Driven by the aim to better understand the physical mechanisms of water vapor annealing process, we performed in situ UV–vis measurements with precise control of RH and temperature. (N.B. Because of the fast kinetics of the annealing process we were unable to conduct *in-situ* AFM and GIXRD measurements.) For *in-situ* spectroscopy, a freshly evaporated film of [Fe(HB(tz)$_3$)$_2$] was placed in a temperature controlled chamber, wherein the RH was changed from 40% to 80% while measuring the absorbance of the film at a sampling rate of 10 Hz. Fig. 4 displays the absorbance change at 318 nm together with the variation in RH for a fixed temperature of 298 K.

The striking observation here is the very abrupt change in absorbance at a RH value of ca. 72%. In a short period of ca. 8 s, the absorbance of the film increases

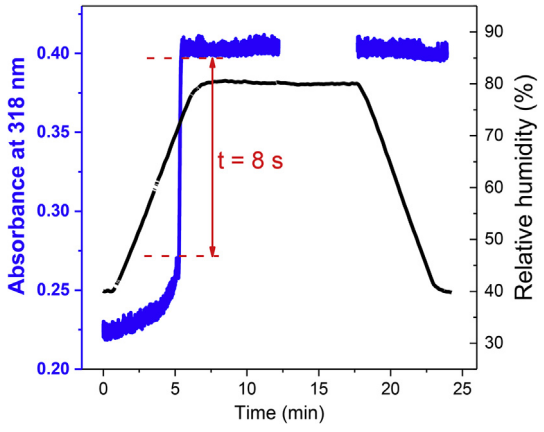

Fig. 4. Absorbance change (baseline corrected) at 318 nm of a [Fe(HB(tz)$_3$)$_2$] thin film as a function of time (blue curve) for increasing and decreasing values of RH (black curve) at a fixed temperature of 298 K. (Note that between ca. 12.5 and 17.5 min, no absorbance data were acquired.)

sharply from 0.27 to 0.40. Before this increase the absorbance change is slow, whereas after the jump the absorbance of the film remains constant for any value of RH, that is, the effect is irreversible. This result was repeatedly observed on fresh films and corroborates our hypothesis that the crystallization of the film during the water vapor annealing occurs by the simultaneous nucleation of a large number of seeds, which then form small, densely packed crystals. The crystalline state reached at the end of the process is extremely stable in air even for repeated thermal cycling. It is worth noting that the humidity treatment results in a solvated film, but the water molecules are desorbed in ambient air *below* the spin transition temperature and they have therefore no effect on the SCO properties [11,13].

Obviously, the water vapor annealing process is influenced by many parameters such as temperature, fluctuations of RH, and exposure time. Regarding this last parameter, we observed that the films remain stable during longer exposure (2 h) to humidity, whereas the other solvent vapors led to the deterioration or even the complete dissolution (or dewetting) of the films. On the other hand, increasing the temperature of the substrate during the water vapor annealing led to decreasing efficiency. At 303 K, the crystallization was still observed, although more gradually. At higher temperatures, however, no absorbance change was detected even for RH 90% indicating less efficient interaction with the water molecules. Furthermore, we observed that keeping the films in ambient air before water vapor treatment leads to an irreversible evolution ("aging") of the films toward an ill-defined semicrystalline state. Fig. 5a depicts the results of water vapor annealing of three similar films with ca. 100 nm thickness, which were beforehand stored in ambient humidity of ca. 57% for 2 min, 15 min, and 2.5 h.

One can notice that the film exposed for 2.5 h displayed a high initial absorbance and did not show any further increase of absorbance with increased RH. This film then revealed different properties compared with the "freshly-treated" samples. Notably, the 10.01° XRD peak intensity of the film exposed to ambient air for 2.5 h is four times less than the peak intensity of the film with only 2 min exposure to ambient air (see Fig. 5b and Table 3). In addition, the relative intensity of other diffraction peaks became more pronounced, indicating that in ambient air, the film evolves in an irreversible manner toward a less crystalline state and less oriented texture. In line with this observation, the spin transition became less complete and less abrupt for prolonged aging in ambient air (Fig. 5c). In addition, the shape of the SCO curves displays an unusual hysteresis over the entire heating–cooling cycle, which indicates continuous sample evolution. We can thus conclude that water vapor annealing (RH > 72%) applied to freshly evaporated $[Fe(HB(tz)_3)_2]$ films provides the best opportunity to achieve an abrupt and complete SCO transition with a high environmental stability, whereas the slow aging of the films at lower RH (i.e., in ambient air) leads to semicrystalline films displaying, as a consequence, ill-reproducible, incomplete and broad spin transitions (see Scheme 2 for a summary of these phenomena).

Table 3
Properties of $[Fe(HB(tz)_3)_2]$ thin films stored in ambient air for different times before humidity treatment.

Aging time	$T_{1/2}$ (K)	ΔT (K)	$Abs_{LS} - Abs_{HS}$	I_{002} (counts)	Abs_{400nm} (baseline corrected)
2 min	339.2	0.9	0.32	11,200	0.09
15 min	339.0	2.4	0.29	7200	0.14
2.5 h	339.5	3.8	0.26	2800	0.20

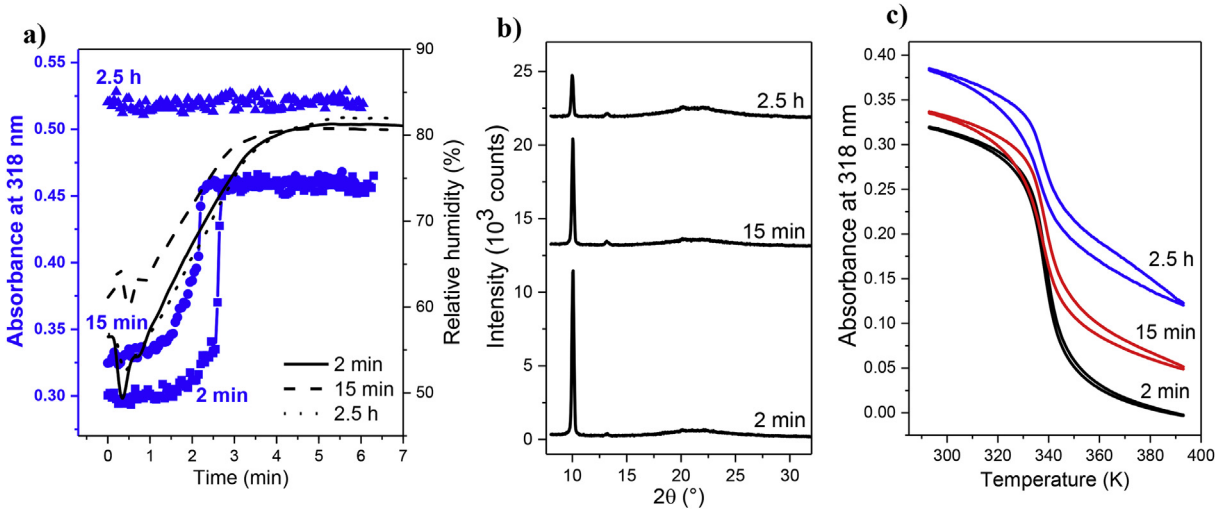

Fig. 5. Investigation of three different $[Fe(HB(tz)_3)_2]$ thin films (each approx. 100 nm thick) stored in air for 2 min, 15 min, and 2.5 h before water vapor annealing: (a) absorbance change ($\lambda = 318$ nm; baseline corrected) during water vapor annealing (i.e., for increasing the RH from the ambient value to 80%). (b) XRD patterns, and (c) temperature dependence of the absorbance (second heating–cooling cycle, $\lambda = 318$ nm, $dT/dt = 1$ K min^{-1}; baseline corrected) after the water vapor treatment.

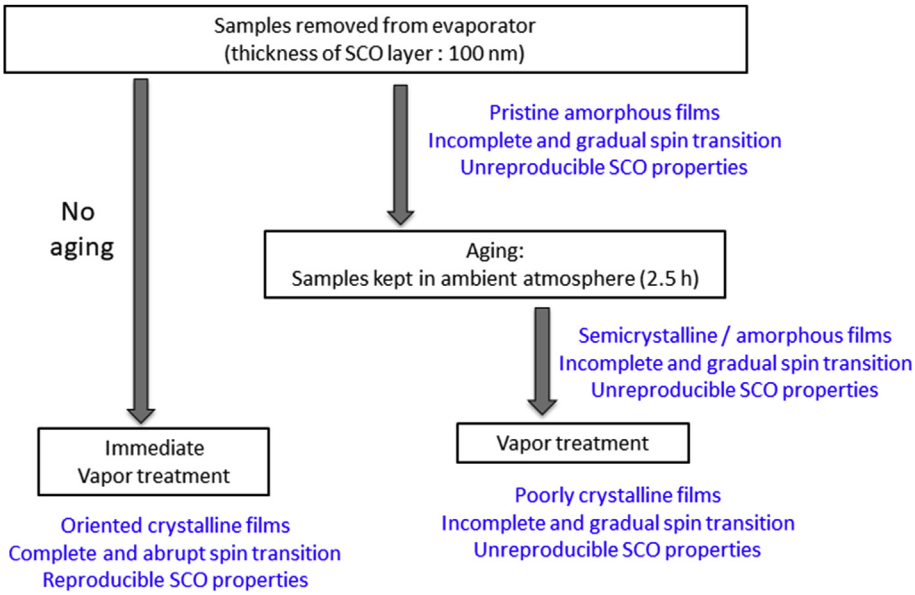

Scheme 2. Summary of the sample evolution depending on the experimental conditions.

4. Conclusions

[Fe(HB(tz)$_3$)$_2$] thermally evaporated thin films were recrystallized by means of SVA using five different solvents: diethyl ether, acetone, dichloromethane, ethanol, and water. GIXRD and UV spectrophotometry showed that the EtO_2-, $(CH_3)_2CO$-, EtOH-, and H_2O-treated films feature highly oriented crystalline structure and an abrupt spin transition at ca. 336 K. CH_2Cl_2 vapor annealed films are less crystalline and do not exhibit a complete spin transition. On the other hand, water appeared to be the only solvent, which provides a smooth and continuous film morphology. The recrystallization process in water was then studied by UV absorption measurements with in situ humidity control. This analysis showed that the crystallization is complete within a few seconds above a threshold humidity value. On the basis of these findings we suggested that the key parameters responsible for film crystallinity and for the control of film morphology could be the hydrogen-bonding ability of the solvents and their solubility parameters. On the whole, SVA provides a simple and fast, yet very powerful method to control crystallinity, texture, morphology, SCO properties, and environmental stability of thin films of [Fe(HB(tz)$_3$)$_2$], which is crucial for the integration in a broad range of nanosized devices. We believe this approach will be increasingly important for the engineering of various SCO films.

Acknowledgments

This work was supported by the European Commission through the SPINSWITCH project (H2020-MSCA-RISE-2016, Grant Agreement No. 734322). The grants of A.B., V.S., and X.T. were financed by the Région Occitanie (no. 15050123), the EMERGENCE@INC208 project, and by the Louisiana State University LSAMP International Research Experience Project for Undergraduates (NSF Grant no. 1560390), respectively. The authors are grateful to Linkam Scientific Instruments for the loan of the RH95 humidity controller.

References

[1] P. Gütlich, H.A. Goodwin, Topics in Current Chemistry. Spin Crossover in Transition Metal Compounds, Springer-Verlag, Berlin, 2004.
[2] A. Bousseksou, G. Molnár, L. Salmon, W. Nicolazzi, Chem. Soc. Rev. 40 (6) (2011) 3313–3335.
[3] M.A. Halcrow, Spin-Crossover Materials: Properties and Applications, Wiley-Blackwell, Chichester, United Kingdom, 2013.
[4] P. Gütlich, A. Hauser, H. Spiering, Angew. Chem., Int. Ed. Engl 33 (20) (1994) 2024–2054.
[5] H.J. Shepherd, G. Molnár, W. Nicolazzi, L. Salmon, A. Bousseksou, Eur. J. Inorg. Chem. (2013) 653–661.
[6] K. Senthil Kumar, M. Ruben, Coord. Chem. Rev. 346 (2017) 176–205.
[7] G. Molnár, S. Rat, L. Salmon, W. Nicolazzi, A. Bousseksou, Adv. Mater. 30 (5) (2018) 1703862.
[8] T. Mallah, M. Cavallini, C. R. Chimie 21 (2018) 1270–1286, https://doi.org/10.1016/j.crci.2018.02.007.
[9] L. Salmon, L. Catala, C. R. Chimie 21 (2018) 1230–1269, https://doi.org/10.1016/j.crci.2018.07.009.
[10] S. Trofimenko, J. Am. Chem. Soc. 89 (24) (1967) 6288–6294.
[11] S. Rat, K. Ridier, L. Vendier, G. Molnár, L. Salmon, A. Bousseksou, T. Leïchlé, L. Salmon, G. Molnár, A. Bousseksou, et al., CrystEngComm 19 (24) (2017) 3271–3280.
[12] K. Ridier, S. Rat, H.J. Shepherd, L. Salmon, W. Nicolazzi, G. Molnár, A. Bousseksou, Phys. Rev. B 96 (13) (2017) 134106.
[13] V. Shalabaeva, S. Rat, M.D. Manrique-Juarez, A.-C. Bas, L. Vendier, L. Salmon, G. Molnár, A. Bousseksou, J. Mater. Chem. C 5 (18) (2017) 4419–4425.
[14] V. Shalabaeva, M. Mikolasek, M.D. Manrique-Juarez, A.-C. Bas, S. Rat, L. Salmon, W. Nicolazzi, G. Molnár, A. Bousseksou, J. Phys. Chem. C 121 (45) (2017) 25617–25621.
[15] M.D. Manrique-Juarez, F. Mathieu, V. Shalabaeva, J. Cacheux, S. Rat, L. Nicu, T. Leïchlé, L. Salmon, G. Molnár, A. Bousseksou, Angew. Chem., Int. Ed. 56 (28) (2017).
[16] M. Mikolasek, M.D. Manrique-Juarez, H.J. Shepherd, K. Ridier, S. Rat, V. Shalabaeva, A.-C. Bas, I.E. Collings, F. Mathieu, J. Cacheux, et al., J. Am. Chem. Soc. 140 (28) (2018) 8970–8979 jacs.8b05347.
[17] V. Shalabaeva, K. Ridier, S. Rat, M.D. Manrique-Juarez, L. Salmon, I. Séguy, A. Rotaru, G. Molnár, A. Bousseksou, Appl. Phys. Lett. 112 (1) (2018), 013301.

[18] L. Poggini, M. Gonidec, J.H. González-Estefan, G. Pecastaings, B. Gobaut, P. Rosa, Adv. Electron. Mater. (2018) 1800204.
[19] J. Zhang, D. Posselt, A. Sepe, X. Shen, J. Perlich, D.-M. Smilgies, C.M. Papadakis, Macromol. Rapid Commun. 34 (16) (2013) 1289–1295.
[20] C. Jin, B.C. Olsen, E.J. Luber, J.M. Buriak, Chem. Mater. 29 (2017) 176–188.
[21] X. Gu, I. Gunkel, A. Hexemer, W. Gu, T.P. Russell, Adv. Mater. 26 (2) (2014) 273–281.
[22] X. Gu, I. Gunkel, A. Hexemer, T.P. Russell, Macromolecules 49 (9) (2016) 3373–3381.
[23] S. Nam, J. Jang, H. Cha, J. Hwang, T.K. An, S. Park, C.E. Park, J. Mater. Chem. 22 (12) (2012) 5543.
[24] Y. Zheng, S. Li, D. Zheng, J. Yu, Org. Electron. 15 (11) (2014) 2647–2653.
[25] G. De Luca, A. Liscio, P. Maccagnani, F. Nolde, V. Palermo, K. Müllen, P. Samorì, Adv. Funct. Mater. 17 (18) (2007) 3791–3798.
[26] L. Wan, S. Ji, C.-C. Liu, G.S.W. Craig, P.F. Nealey, Soft Matter 12 (11) (2016) 2914–2922.
[27] A.O.F. Jones, Y.H. Geerts, J. Karpinska, A.R. Kennedy, R. Resel, C. Röthel, C. Ruzié, O. Werzer, M. Sferrazza, ACS Appl. Mater. Interfaces 7 (3) (2015) 1868–1873.
[28] H.M.A. Ehmann, R. Baumgartner, B. Kunert, A. Zimmer, E. Roblegg, O. Werzer, J. Phys. Chem. C 118 (24) (2014) 12855–12861.
[29] H.M.A. Ehmann, A. Zimmer, E. Roblegg, O. Werzer, Cryst. Growth Des. 14 (3) (2014) 1386–1391.
[30] F. Borgatti, P. Torelli, M. Brucale, D. Gentili, G. Panaccione, C. Castan Guerrero, B. Schäfer, M. Ruben, M. Cavallini, Langmuir 34 (12) (2018) 3604–3609.
[31] Y. Marcus, Chem. Soc. Rev. 22 (6) (1993) 409.
[32] V. Davesne, M. Gruber, M. Studniarek, W.H. Doh, S. Zafeiratos, L. Joly, F. Sirotti, M.G. Silly, A.B. Gaspar, J.A. Real, et al., J. Chem. Phys. 142 (19) (2015) 194702.
[33] S. Nam, D.S. Chung, J. Jang, S.H. Kim, C. Yang, S.-K. Kwon, C.E. Park, J. Electrochem. Soc. 157 (1) (2010) H90.